Pre- and Post-processing Strategies for Generic Slice-wise Segmentation of Tomographic 3D Datasets Utilizing U-Net Deep Learning Models Trained for Specific Diagnostic Domains

Gerald A. Zwettler[1,2], Werner Backfrieder[3] and David R. Holmes III[1]
[1]*Biomedical Analytics and Computational Engineering Lab, Department of Physiology and Biomedical Engineering, Mayo Clinic College of Medicine, 200 First St. SW, 55905 Rochester, MN, U.S.A.*
[2]*Research Group Advanced Information Systems and Technology (AIST), Department of Software Engineering, University of Applied Sciences Upper Austria, Softwarepark 11, 4232 Hagenberg, Austria*
[3]*Medical Informatics, Department of Software Engineering, University of Applied Sciences Upper Austria, Softwarepark 11, 4232 Hagenberg, Austria*

Keywords: Deep Learning, U-Net, Model-based Segmentation in Medicine, Computed Tomography.

Abstract: An automated and generally applicable method for segmentation is still in focus of medical image processing research. Since a few years artificial inteligence methods show promising results, especially with widely available scalable Deep Learning libraries. In this work, a five layer hybrid U-net is developed for slice-by-slice segmentation of liver data sets. Training data is taken from the Medical Segmentation Decathlon database, providing 131 fully segmented volumes. A slice-oriented segmentation model is implemented utilizing deep learning algorithms with adaptions for variable parenchyma shape along the stacking direction and similarities between adjacent slices. Both are transformed for coronal and sagittal views. The implementation is on a GPU rack with TensorFlow and Keras. For a quantitative measure of segmentation accuracy, standardized volume and surface metrics are used. Results *DSC=97.59*, *JI=95.29* and *NSD=99.37* show proper segmentation comparable to 3D U-Nets and other state of the art. The development of a 2D-slice oriented segmentation is justified by short training time and less complexity and therefore massively reduced memory consumption. This work manifests the high potential of AI methods for general use in medical segmentation as fully- or semi-automated tool supervised by the expert user.

1 INTRODUCTION

Automated and precise segmentation of anatomical structures for computer-assisted diagnostics is still field of ongoing research. Only for particular domains, off-the-shelf applications are available (Christensen and Wake, 2018) but generally computer-aided diagnostic is achieved in a user-centric process utilizing frameworks providing tools for semi-automated processing (Strakos et al. 2015). The manual processing of the datasets thereby necessitates a lot of experience in both, the technical and the medical domain and is exposed to subjective processing, even if following a rather standardized segmentation process (Zwettler et al. 2013).

1.1 Medical Background

The precise segmentation of specific anatomical structures from 3D data forms the basis for quantitative analysis in computer-assisted diagnostics. The quantitation aspect is relevant for assessing disease progression or general scoring (Aggarwal et al. 2011). Based on segmented anatomical structures, the visualization and inspection in 3D, as well as utilization in AR and VR environments becomes feasible. Segmentations are further relevant for surgery planning, building up anatomical atlas models, evaluating image acquisition protocols or as input data for nowadays widely available 3D print (Squelch 2018).

1.2 Sate of the Art

Since the appearance of the first CT scanners, in the early 1970s, intensive research in the field of medical image processing targeting at fully automated segmentation approaches has been initiated and is still going on.

Zwettler, G., Backfrieder, W. and Holmes III, D.
Pre- and Post-processing Strategies for Generic Slice-wise Segmentation of Tomographic 3D Datasets Utilizing U-Net Deep Learning Models Trained for Specific Diagnostic Domains.
DOI: 10.5220/0008932100660078
In *Proceedings of the 15th International Joint Conference on Computer Vision, Imaging and Computer Graphics Theory and Applications (VISIGRAPP 2020) - Volume 5: VISAPP*, pages 66-78
ISBN: 978-989-758-402-2; ISSN: 2184-4321

A priori knowledge about the target shape, lead to deformable models (McInerney and Terzopoulos 1996). With statistical shape (Cootes et al. 1992), adaptive models are calculated from a large set of reference datasets with corresponding reference positions, thus representing the statistical shape variability of the target anatomical structure in a sophisticated way. Statistical Shape models allow for a very compact representation of the target's structure due to PCA but the precise and generic determination of corresponding landmarks is still unsolved and necessitates specific approaches in particular diagnostic domains. Incorporating the input dataset intensity profiles besides shape, Active Appearance Models (Cootes et al. 1998) can be trained for automated segmentation in specific anatomical domains but attracted interest and significance in a non-diagnostic domain, namely human face comparison and recognition.

In recent years, improvements in GPU speed, massive efforts in AI research of large companies and availability of machine learning frameworks such as Tensorflow to the research community were the trigger for significant improvements in Deep Learning and to allow for technical implementation of some concepts, since then only theoretically documented. The most significant developments are thereby Feed Forward networks with several hidden layers that are applicable in many computer vision and also speech recognition tasks. Nevertheless, Feed Forward networks are also applied for medical multi-modal image fusion (Zhang and Wang 2011). The concept of self-organizing neural networks first introduced by Kohonen (Kohonen 1995) for clustering in complex domains was successfully applied to classification of renal diseases too (Van Biesen 1998). With recurrent neural networks and long/short-term-memories (LSTM) (Hochreiter and Schmidhuber 1997) semantic processing of input data sequences as relevant for OCR and voice analysis, c.f. DeepVoice, became feasible (Arik et al. 2017). One of the most significant developments in Deep Learning in recent years are convolutional neural networks, training kernels and weights of multi-resolution filter pyramids and thus clearly outperforming classic convolutional-layer based approaches such as Haar Cascades (Viola and Jones 2001). Some of the most relevant CNN architectures are LeNet, AlexNet, GoogLeNet or ResNet showing more than 1200 layer. New fields of application opened generative adversial networks (GAN) (Goodfellow et al. 2014). It is applied for mimicking of natural data in domains as generating paintings, hand written letters or medical data (Yi et al. 2019). The latter are used for automated liver segmentation (Yang et al., 2017) or generation of test data to prevent from over-fitting (Frid-Adar 2018).

1.3 Related Work

The U-Net architecture was initially developed for 2D cell border classification (Ronneberg et al. 2014) but soon transformed to processing 3D data too (Cicek et al. 2016), applicable for brain tumor segmentation (Amorim et al. 2017), liver segmentation (Meine et al. 2018) and various other medical diagnostic domains.

Recent notable advances in 3D U-Net architectures are 3D dilated convolution kernels to significantly speed-up the processing and allow for real-time application (Chen et al. 2019) as well as generic models for semantic segmentation on different imaging modalities and anatomical structures (Huang et al. 2019).

1.4 Generic Deep Learning Models

In this work, several approaches for utilizing conventional U-Net architectures for slice-wise processing of tomographic 3D datasets are presented. Due to the utilized pre-processing strategy with ROI selection and adjusting the intensity profile, the approach evaluated on liver CT datasets is applicable to different domains like lung, kidney or other modalities such as brain MRI too.

Besides a sufficient amount of at least 100 volumes along with precise reference segmentations, for the generic segmentation approach no additional domain-specific knowledge is incorporated.

Due to the slice-wise processing, important aspects of the 3D dataset such as position within the patient get lost. In this work several strategies are adressed and evaluated to utilize positional information for the slice-wise processing.

2 MATERIAL

For this research work, the liver datasets from the *Medical Segmentation Decathlon* database (Simpson et al., 2019) are utilized for training, validation and test. The use of the database is restricted to the 131 liver datasets that are provided together with reference segmentations as ground truth. All 3D volumes are available in *NIFTI1* image format (DFWG, 2005), a modification of the *Analyze 7.5 format* (BIR, 1986). The medical image analysis software *Analyze* (Robb et al. 1989) is utilized to convert the datasets from *NIFTI1* to Analyze 7.5 and to perform the data preparation and pre-processing subsequently described in section 2.2.

2.1 Analytic Inspection of the Task03_Liver Datasets

The 3D volumes are available as axial slices of matrix size 512×512 with an average number of slices $\mu_{sliceCnt}$=447.62±275.25 [74;987]. The iso-spacing in x/y-direction is given with $\mu_{spacingXY}$=0.793±.118 [.1557;1.000] and the inhomogeneous slice thickness is described with $\mu_{spacingXY}$=1.506±1.177 [.699;5.000].

The intensities of the CT slices range between μ_{intMIN}=-1103.26±204.93 [-2048;-1000] to μ_{intMAX}=3334.70±3566.96 [1023;27748]. The vendor-related suspicious low and high values are not further addressed as they are out of the relevant intensity context for the liver segmentation domain.

The reference segmentations provided for the liver datasets represent a three-class non-overlapping discrimination of the volume, namely *background* (0), *liver* (1) and *liver tumour* (2) as shown in Fig.1 for slice 417 of dataset #0.

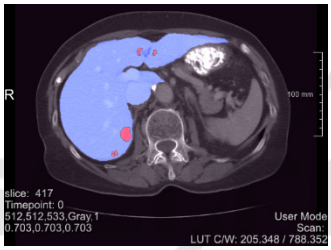

Figure 1: Med Decathlon slice 417 of liver dataset #0 with parenchyma (blue) and the tumour (red) respectively.

2.2 Data Preparation and Pre-processing

In this work a binary segmentation of the liver parenchyma is the objective target. Thus, the ground truth for liver and tumour areas are merged leading to an encapsulated liver shape.

To balance the significant mismatch in slice thicknesses, the z spacing is adjusted to the x/y inter-slice spacing utilizing cubic interpolation for the intensity dataset and shape interpolation (Rajagopalan et al. 2003) for the binary reference masks. In case of the slice thickness being below the in plane resolution, the data remains unchanged to conserve the axial slices at extent 512×512.

Due to the up-sampling, the number of slices is increased to $\mu_{sliceCnt}$=639.55±248.77 [74;998]. Analysing the extent of the liver within the particular datasets, the size of the enclosing ROI extent is given with $\mu_{widthLiver}$=285.02±42.54, $\mu_{heightLiver}$=246.50±31.83 and $\mu_{widthLiver}$=208.84± 57.87. To process the input data almost at original resolution and nevertheless limiting the size of the model to be trained, all axial slices are scaled to an extent of 352×288 pixels, thereby conserving the aspect ratio and placing the image content at the centre. A total number of 27,358 slices is available, segregated into train, validation and test datasets.

Besides normalization with respect to the extent, the intensity profile is adjusted utilizing a scalar transfer function similar to common windowing. Based on the average intensity μ_{liver} and σ_{liver}, the transfer function is applied according to Eqn. (1) for scale $s = \frac{115}{3 \cdot \sigma_{liver}}$ to restrict all values to a range of [12;243].

$$T(a_i) = \begin{cases} MAX(127 - |a_i - \mu_{liver}| \cdot s, 0) & a_i \leq \mu_{liver} \\ MIN(127 + |a_i - \mu_{liver}| \cdot s, 255) & a_i > \mu_{liver} \end{cases} \quad (1)$$

The scale ratio thereby does not transform values to full range of [0;255] to allow for some adaptability with respect to data augmentation. For training, μ_{liver} and σ_{liver} are derived from statistical analysis with given binary reference segmentation mask, while for testing the range is derived from manual windowing.

As shown in Fig. 2, all axial slices are scaled to the target extent of 352×288 pixels with the intensity profile of the target structure normalized around midst position 127 of utilized data type *unsigned char* in terms of data normalization, see Fig. 2 for slice 100 of pre-processed dataset #0.

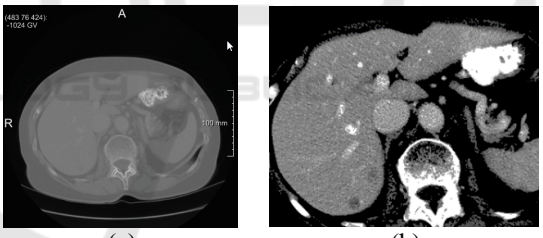

(a) (b)

Figure 2: The original slice 424 of dataset #0 (a) is cropped according to reference segmentation mask with the average pixel intensity of the liver parenchyma.

The given reference segmentations are of acceptable accuracy and thus stay untouched with one exceptional case, namely dataset #102 where around slice 323 there is an invalid small blob classified offshore the parenchyma that is removed.

3 METHODOLOGY

For liver segmentation based on tomographic 3D volume data, several approaches for slice-wise processing are evaluated and finally combined in a hybrid model. For the segmentation task a U-net

architecture comprising 5 levels of hierarchy is adjusted to input image size of 352×288 pixels for axial slices, see Fig. 3. To prevent implicit shrinking by each convolution operation, padding is applied, thus ensuring intermediate image size reduced by a factor of two at each hierarchy level, namely 176×144, 88×72, 44×36 and 22×18 respectively. The network complexity is manifested by 31,031,685 trainable parameters with kernel size 3×3 and considering the bias parameters for each of the in total 23 layers.

3.1 Data Augmentation

With the liver dataset from the *Medical Segmentation Decathlon* database only 131 tomographic CT volumes are available. Nevertheless, as the volume is processed in a slice-wise manner, the CT volumes result in at least 27,358 axial slices available for training, validation and test. Due to the high resolution, differences between neighbouring slices are low and thus redundancy is present in the dataset. Thus, data augmentation is needed to enrich the number of input slices to prevent from over-fitting at higher epoch counts and to reduce the gap between training and testing accuracy.

Data augmentation is implemented in an original way to keep full control of the nature of the artificial images generated compared to out of the box Keras/Tensorflow functionality. The following parameters are used to manipulate the slices chosen for the current batch and thus to enrich the amount of data available for training:

- *transX* and *transY:* translation in x-direction and y-direction of the current slice
- *rot:* rotation around the image center
- *intMul:* linear scale of the image intensities leading to brighter or darker pixel values within the borders of the windowing range
- *intAdd:* additive manipulation of the intensities within the window, leading to a uniform shift for full scalar range

For all of these parameters, a valid range is configured a priori. The parameter set to apply for a particular image is then given as randomly selected values (uniform distribution) within the valid range of the augmentation parameters.

Pixel values of the augmented image are thereby calculated as shown in Eqn. (2).

$$imgA(x,y) = img(x',y') \cdot (1 + (rnd - 0.5) \cdot intMul) + (rnd - 0.5) \cdot \text{intAdd} \quad (2)$$

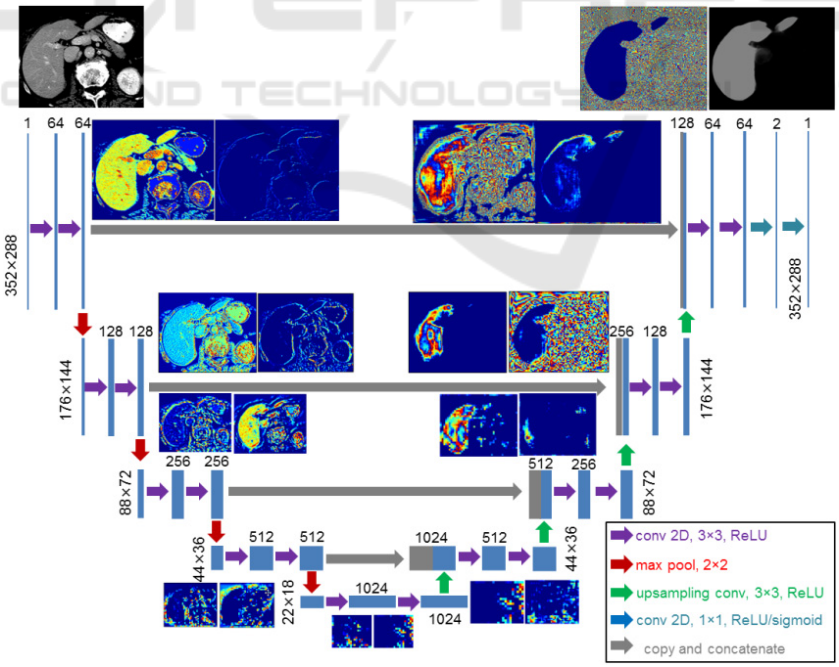

Figure 3: Network layout of the U-Net architecture utilized in this paper adapted from (Ronneberg et al. 2015). The intermediate results on each of the five hierarchy layer are visualized for slice 72 of dataset #0. At full resolution of 352×288 two layers with 64 convolution kernels are applied while after reducing the size to 176×144 two layers with 128 convolution kernels each are applied. To reconstruct the original size, four concat operators and up-sampling are applied.

$$\begin{bmatrix} x' \\ y' \end{bmatrix} = \begin{bmatrix} x - \frac{width}{2} \\ y - \frac{height}{2} \end{bmatrix} \cdot \begin{bmatrix} cos\theta & -sin\theta \\ sin\theta & cos\theta \end{bmatrix} + \begin{bmatrix} (rand - 0.5) \cdot transX \\ (rand - 0.5) \cdot transY \end{bmatrix} \quad (3)$$

with rnd in $[0.0; 1.0]$ and $\theta = (rnd - 0.5) \cdot rot$.

A drawback of common data augmentation is the loss of image information when rotating and translating the image content while introducing background regions with lack of information confusing the model training process. To adress this problem and to dampen the effects, a safety margin of `paddingOffset =10` is used to provide a surrounding frame with original image data to use for the augmented images, see Fig. 4.

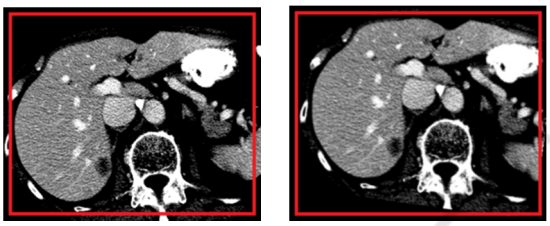

(a) (b)

Figure 4: Although the axial slices utilized are of size 352×288, due to the *paddingOffset* the virtual image size is 372×308 thus introducing a safety margin for transformations (a). With `transX=15.5`, `transY=-23.8` and `rot=8.1` the relevant image content is still within the processed as visible for the sinister rib cage (b).

3.2 Deep Learning based Classification

3.2.1 Classification of Axial Slices

In a straight-forward approach the tomographic input datasets are sliced in axial direction to provide one-channel input tensors of size 352×288 for the *modelAxial.h5* ***axial*** U-Net (*ax*) weights to be trained. Due to the a priori defined ROI of the parenchyma area, the axial parenchyma shape grows and shrinks in caudal-to-cranial direction with moving position according to a significant trend. Nevertheless, this positional information within the slices is not utilized in this approach.

According to the chosen pre-processing, the aspect ratio of the axial slices is conserved with the width, height scaled to the target tensor size utilizing cubic interpolation. In z-direction there is no interpolation required. All axial slices are varied with respect to data augmentation parameters $[16, 16, 10, .1, 30]$ for *transX, transY, rot, intMul* and *intAdd respectively*.

For model training, a learning rate of $lr = 5 \cdot 10^{-6}$ is configured for the *Adam Optimizer* (Kingma and Ba 2014) with $beta1 = 0.9$, $beta2 = 0.999$ and $epsilon = 10^{-8}$ using *cross-entropy* as loss. The training runs for *200* epochs at most using $batchSize = 32$ and $patience = 12$ preventing from pre-mature stopping (validation loss).

3.2.2 Discrete Axial Model for Specific Z-ranges within the ROI

With the model *modelAxial.h5* neither 3D information nor the characteristic axial liver shape according to the position within the ROI are incorporated. Especially in the caudal and cranial section of the ROI the parenchyma size is low and varying intensity profiles observed. Thus, the position within the ROI, denoted as *sliceRatio* with values scaled to $[0; 1]$ should be incorporated too.

For the chosen U-net architecture, it is hard to provide the relevant *sliceRatio* parameter as additional input to the network. It is possible to attach a FCN layer with medium depth at the end of U-Net probability mask classification to use the *sliceRatio* parameter for automatic derivation of the locally best threshold value for final binarization of the segmentation. Nevertheless, there the positional impact would be marginal.

As both the shape and position of the parenchyma areas vary heavily within an entire 3D volume, splitting the slice range into smaller sections increases the local homogeneity at the cost of reduced amount of training data, see Fig. 5.

To smooth transitions, the reduced amount of training data for each of the sections as well as the sharp border areas between them, the segments are defined to overlap by *0.05* with *[0;0.25[, [0.15;0.45[, [0.35;0.65[, [0.55;0.85[* and *[0.75;1.00]* for the sections 1-5 respectively.

To further utilize the predictability of neighbouring segments close to the border sections, the final result is combined in a linear interpolation way as shown in Eqn. (4) with only the at most two sections neighbouring the particular *sliceRatio* sr_j are incorporated for number of classes $nc = 5$ and model predictions $pred_i$.

$$img_{res,j} = \sum_{i=1}^{5} pred_{i,j} \cdot weight_{i,j} \text{ with}$$

$$weight_{i,j} = \frac{\left| \left(\frac{1}{nc}^2 - \left(min\left(\frac{1}{nc}, \left| sr_j - \frac{1}{2 \cdot nc} + i \cdot \frac{1}{nc} \right| \right) \right)^2 \right|}{\frac{1}{nc}^2} \quad (4)$$

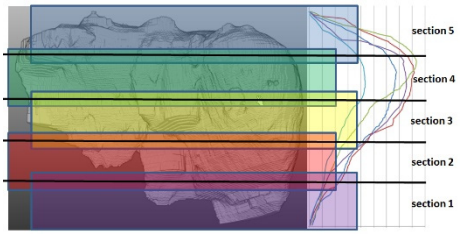

Figure 5: The axial slice stack is devided into overlapping *sections 1-5*. As shown on the right chart, the position-related trend in size for the first n=5 datasets is highly correlated and thus motivates splitting into model sections.

3.2.3 Slice Propagation Incorporating Neighbouring Results

Due to the high inter-slice-resolution of the employed CT data, neighbouring slices show a high correlation with respect to position, size and orientation of the segmentations. Incorporating this given fact, the actual slice segmentations are expected to get stabilized. A similar semantic plausibility check is used with LSTM deep learning for natural language processing or for robust video object retrieval. Certainly, LSTM concepts would be applicable too but enriching the neighbouring slices with the right amount of uncertainty at all memory layers is a challenging task.

Consequently, another 2D U-Net approach is chosen and enriched with the neighbouring slices. Besides the input $slice_n$ to be segmented, also autonomous segmentation results of the previous and next slice as $seg(slice, modelAxial)_{n-1}$ and $seg(slice, modelAxial)_{n+1}$ are added to the input tensor that is reshaped to $(1, 288, 352, 3)$ extent similar as applicable for RGB images, c.f. Fig. 6.

A crucial aspect is how to define the neighbouring slices for training. With the ground truth provided, the influence of the particular intensity profile slice is marginalized, thus only the proximate slices are utilized.

The data augmentation for this 3-slice concept is of high importance. The transformation of the mid slice is performed with the same parameter set $[16, 16, 10, .1, 30]$ as used in section 3.1. To conserve the inter-slice-correlation it would neither be a good idea to randomly transform the proximate slices nor to move them along with the mid slice to sustain a small but crucial level of variability. Thus, for the previous and next slice, a ¼ of the mid slice data augmentation range is utilized and applied relative to the mid slice transformation.

With the presented 3-slice model of $prediction(n-1)$, $orig(n)$ and $prediction(n+1)$ denoted as ax_{pop}, the results of a first run can be improved by bottom-up and top-down processing. Furthermore, the slice-wise propagation opens rich possibility for manual adjustment of the results.

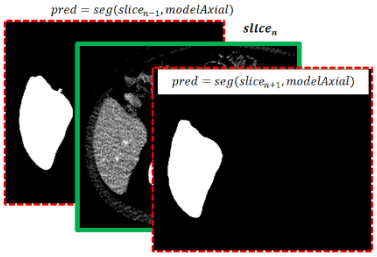

Figure 6: The training tensor for the mid slice is enriched by neighbouring single-slice predictions.

3.2.4 Incorporating Axial and Sagittal Views for Overall Classification Building up a Hybrid Position-based Model

The drawback of slice-wise data processing are the outer sections, where the target structure continuously vanishes in mass. For the axial slices, this is the case in the top and bottom rows. To overcome this limitation, it makes sense to incorporate sagittal and coronal slices too. Although the sagittal and coronal slices show weaknesses in the left/right and front/back areas respectively, with respect to the overall information a significant gain is expected. Axial slices are transformed to sagittal (256x376) and coronal (256x308) with z-dimension scaled to 256 for each of the 3D datasets. Two U-net models, ***sagittal*** (ax_s) and ***coronal*** (ax_c), are trained and applied as described in section 3.2.1 with results back-transformed to axial view. In Fig. 7 the preparation of segmentation results for axial, sagittal and coronal can be seen in the *classify*-section.

The 3-slice model ax_{pop}, incorporating neighbouring slices and thus a marginally perspective aspect is expected to be capable of further improving slice-by-slice results, c.f. *improve* section of Fig. 7. With ax_{pop} applied to reconstructions from sagittal and coronal, axial segmentation information is thereby already incorporated lowering the benefit for combination of the three orthogonal views. Thus, sagittal and coronal predictions are improved with specific 3-slice models denoted as $ax_{spopSAG}$ and $ax_{spopCOR}$ respectively, see Fig. 7.

Now, as for each slice a good segmentation result from axial, sagittal and coronal view is achieved, they get *combined* for the final result.

The most straight forward approach thereby is averaging of the three particular slices, denoted as $AVG_{a\prime,c\prime,s\prime}$. As for the border areas two of three views are

expected to contribute good results, averaging or majority voting seem to be a functional approach.

Alternatively, a 3-layer U-Net model can be trained as decision tree, denoted as $model_{a',c',s'}$.

A third approach ($PosW_{a',c',s'}$) for combining the orthogonal slices focuses on the position-based evaluation of the prediction accuracy of the axial, sagittal and coronal models calculated from pixel-wise error as a normalized volume of size 100×100×100. Smoothing (*Gaussian kernel, r=1, 8 runs*) is applied to get a dense weight-map for position-dependent accuracy of axial, coronal and sagittal slices.

4 IMPLEMENTATION

For the manually performed pre-processing steps such as converting the image type, resampling to isotopic voxels as well as for visualization of the results the image processing frameworks and tools Analyze, MeVisLab and ImageJ are utilized.

The model training and testing is implemented in Python version 3.7.3 with separate parameterizable scripts for the various process steps using Tensorflow 2.0 beta together with Keras.

The Python image processing is largely built upon OpenCV or numpy for fast matrix operations.

To provide the model with training data, a `DataGenerator` class is derived from `Sequence` base class.

With a data generator, the batches can be loaded from the file system on demand and one gets full control on the data augmentation and on the batch-randomization.

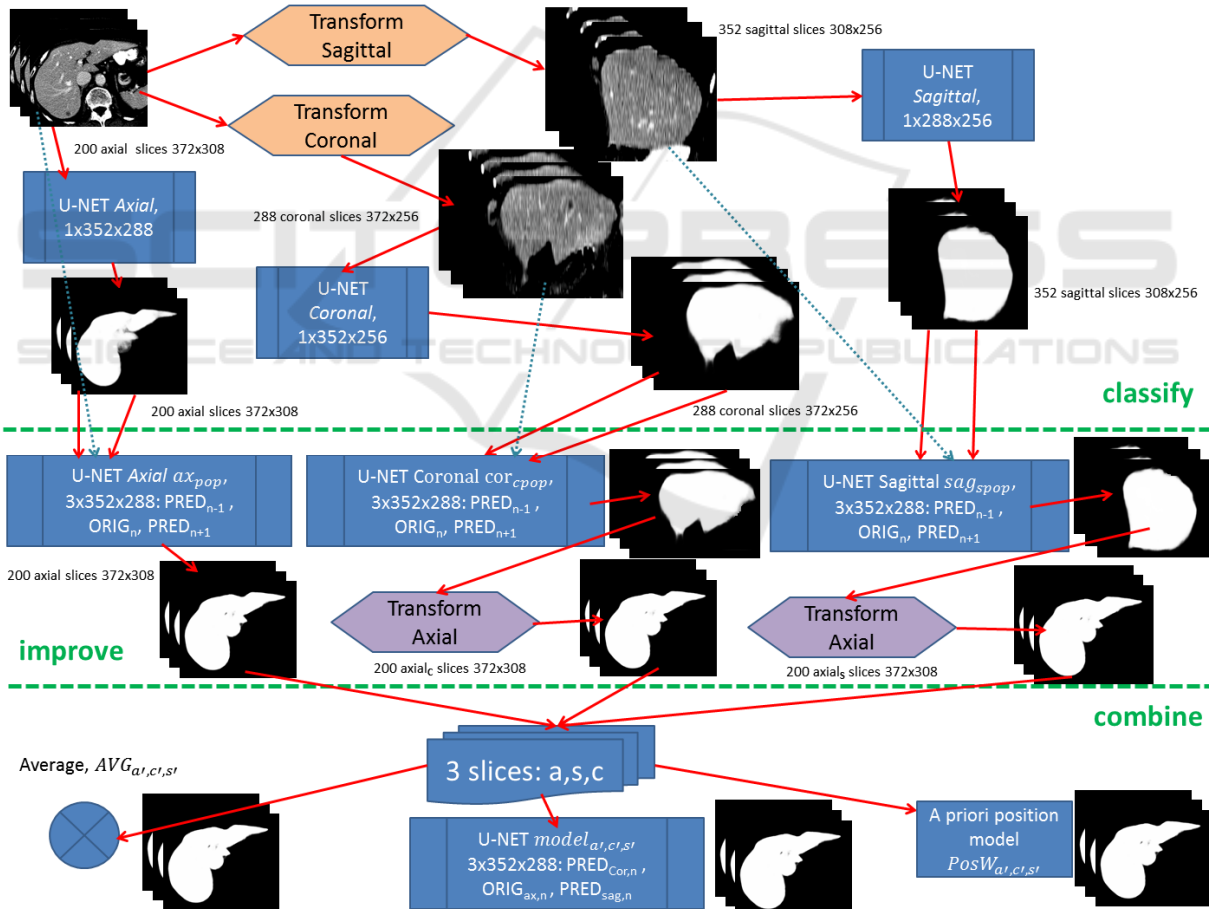

Figure 7: Axial slices are first transformed into sagittal and coronal views too, all to get classified by an individual U-Net. After this *classification* section, results can further be *improv*ed by using a generic 3-slice U-Net (ax_{pop}) after reconstruction to axial view or specific ones (sag_{pop}, cor_{pop}) prior to axial reconstruction. The improved results finally get *combine*d by one of the three proposed strategies, averaging, U-net trained for merging or a position-based weighting algorithm.

5 RESULTS

5.1 Evaluation Metrics

For evaluation, in this work the same metrics as proposed by the medical decathlon challenge are used (MedDecathlon 2018). These are the *Sørensen-Dice coefficient* (DSC)(Dice, 1945) for evaluation of the spatial overlap and the *normalized surface distance* (NSD) (Laplante, 2019) evaluating the spatial proximity of test and reference shape to compare. Additionally, the Jaccard index (Jaccard, 1912) as a stricter metric for area match compared to the Dice coefficient is evaluated too to allow for comparability with further research papers. The metrics are calculated according to Eqs. (5)-(7) for foreground reference segmentation R and foreground test region S of image I with $R \subseteq I, S \subseteq I$ and pixels $(x, y) \in R \cup S$.

$$DSC(R,S) = \frac{2 \cdot |R \cap S|}{|R| + |S|} \tag{5}$$

$$NSD(R,I) = 1 - \frac{\sum_{x,y}[\![R_{x,y} \neq I_{x,y}]\!] \cdot D(R)_{x,y}}{\sum_{x,y} D(R)_{x,y}}, \quad D_{x,y}(R) = dist_{Euc}(surf(R)) \tag{6}$$

$$JI(R,S) = \frac{|R \cap S|}{|R| + |S| - |R \cap S|} \tag{7}$$

Metric $NSD(R,I) \in [0;1]$ thereby calculates for error pixels the distance to the correct border of the reference shape and normalizes with pixels in $R \cup S$.

For the overall accuracy of a dataset, i.e. 3D volume, the metrics DSC, NSD and JI are caclulated by summing up the FP, FN and correct results of all the slices. To adress the statistics per slice, for the same metrics a median slice accuracy is evaluated per dataset denoted as DSC_{med}, NSD_{med} and JI_{med} respectively. Testing on several 3D volumes, the partciular results of the six mentioned metrics are statistically analyzed too for getting an overall evidence.

5.2 Hardware Infrastructure

All of the process steps discussed in this paper, namely data preparation, pre-processing, model training and validation/test are performed on a *Colfax SX9600 GPU Rack* with 2×I*ntel Xeon Gold 6148 2.4GHZ* processors and 768GB of DDR4 memory with 2667MHZ clock frequency split into 24 partitions of 32GB each. The system runs *CentosOS 7.6* operating system and provides for fast tensor calculation 8 GPU cores, namely 4× *NVIDIA Volta Titan V 12G* and 4× *NVIDIA Tesla V100 32G*.

5.3 Results on Pre-processing and Data Augmentation

The safety margin of 10 pixels used to enlarge the input axial slices from 352×288 to 372×308 successfully helped to prevent from black-areas due to rotation and translation outside the image borders for the effective image range. The intensity profile manipulation for the data augmentation process does not result in a value overflow, see Fig. 8.

To preserve the binary reference segmentation masks, as interpolation strategy the modes *Area* and *Nearest Neighbour* are to be utilized only.

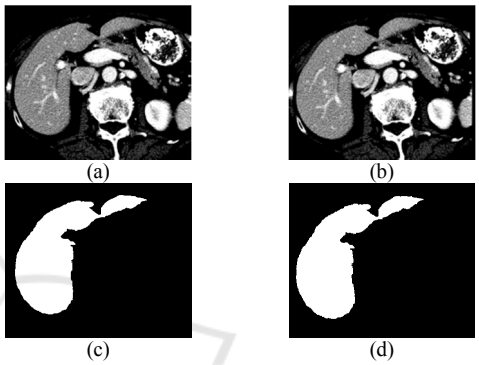

Figure 8: Axial slice 276 (a) and reference segmentation (c) get transformed by `transX=-6.64`, `transY=3.51`, `rot=3.00`, `intMul=1.02` *and* `intAdd=-5.74` (b), (d).

5.4 Slice-wise Classification Utilizing a Single Model

The following axial, sagittal and coronal models are trained with 22,000 (axial), 40,000 (sagittal) and 32,000 (coronal) augmented datasets while validation is performed with the remaining datasets, namely 4,858 (axial), 8,232 (sagittal) and 7,848 (coronal). The imbalance in train and test data results from different dataset dimensionality in the main viewing directions and is implicitly balanced utilizing data augmentation.

For results of the evaluation metrics on the axial, sagittal and coronal model, c.f. Table 1. Furthermore, the models ax_s and ax_c are evaluated after reconstruction and resampling from sagittal/axial to axial slices.

Although the axial, cornal and sagittal model show similar accuracy, their particular strength is located in various sections as shown in Fig. 9. The axial model is weak in the caudal sections but outperforming in the cranial sections.

Table 1: Results for the particular slice-wise models evaluated on the test datasets.

model	DSC	DSC_{med}	JI	JI_{med}	NSD	NSD_{med}
ax	96.2	96.6	92.6	93.4	98.2	99.0
ax_s	96.8	96.9	93.8	93.9	96.2	99.3
ax_c	96.5	96.5	93.2	93.3	97.9	98.6

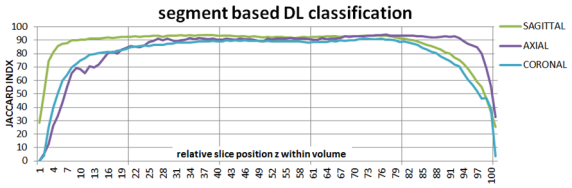

Figure 9: JI metric evaluated for axial, sagittal and coronal model per 1% intervals with respect to relative z-position within the volume.

The training process for the final axial model is shown in Fig.10 (a) while in Fig.10 (b) an premature stagnation with identical settings is visible. With each epoch on full training data lasting for *35:10 minutes* the overall training of a large model took *15-20 hours*. In contrast, model evaluation takes place in millisecond range and is only affected by file loading and pre-processing demand.

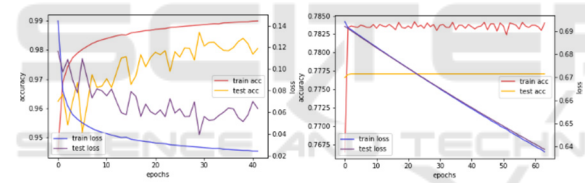

(a) (b)

Figure 10: While in (a) the axial model approaches good results within 36 epochs, depending on the initial random batch and random the training gets early stuck in about 50% of the cases (b).

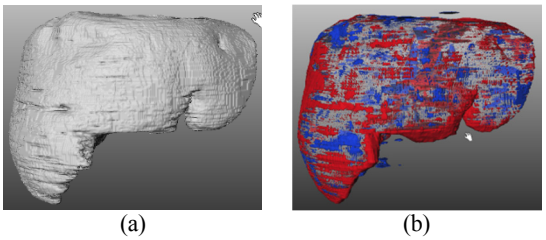

(a) (b)

Figure 11: Correctly segmented liver area for dataset #101 in (a) and FP, FN visualization at surface and *vena porta* areas in (b).

The achievable segmentation accuracy is visualized for dataset #111 in Fig. 11 with the matching volume in (a) and the FP and FN areas in blue and red respectively. Axial segmentation results are rather weak in the caudal and cranial areas, see Fig. 12. This deficiency is easily levelled by incorporating sagittal and coronal too, see Fig. 13.

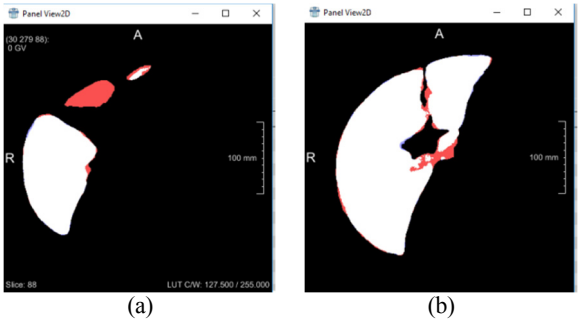

(a) (b)

Figure 12: Axial view of segmentation mismatch of slice 88 and 135 of dataset #111 for model *ax* (a-b). In caudal direction the starting slices of new morphological islands sometimes stay unclassified.

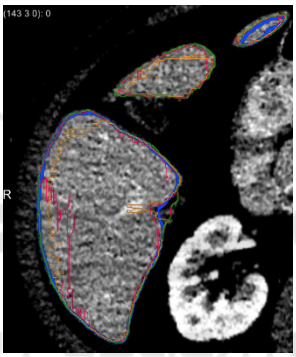

Figure 13: Axial view of segmentation mismatch of slice 88 of dataset #111 with ground truth (green), axial (blue), sagittal (red) and coronal (orange) incorporating the midst parenchyma part (red FN region in Fig. 12 (a)) in caudal direction in contrast to the axial result.

5.5 Classification with Discrete Axial Models for Specific Z-ranges

Results on the section-based models are listed in Tab. 2. As the training data of 22.000 slices gets split up into 5 sections, the quality of these specific models are marginally below the full axial model *ax*. Only if the axial model is trained with a reduced amount of data too for reason of compensation (axial small, ax_{small}), the section models are significantly outperforming. The mode with linearly combining the classification results of the neighbouring sections for a particular slice (e.g. $ax_{1,nb}$) outperform the use of only the nearest section (e.g. ax_1).

Table 2: Section based evaluation of various models, namely full axial model ax trained with 22,000 datasets, axsmall only trained with 4,400 datasets such as the section models ax1- ax5. Model axnb incorporates neighbouring sections for linear interpolation.

S	model	DSC	DSC_{med}	JI	JI_{med}	NSD	NSD_{med}
1	ax	89.8	93.0	81.5	86.9	88.1	96.4
	ax_{small}	67.0	62.5	50.3	45.5	41.9	45.2
	ax_1	87.4	88.4	77.6	79.3	82.2	89.5
	$ax_{1,nb}$	88.0	89.3	78.5	80.6	83.6	90.9
2	ax	96.2	97.0	92.6	94.2	97.7	99.3
	ax_{small}	86.5	88.2	76.2	78.9	85.5	88.7
	ax_2	96.0	97.0	92.2	94.1	97.3	99.3
	$ax_{2,nb}$	96.2	97.2	92.6	94.5	97.6	99.4
3	ax	96.2	96.7	92.6	93.5	98.2	99.1
	ax_{small}	87.3	88.1	77.5	78.7	87.3	89.9
	ax_3	96.9	97.2	93.9	94.6	98.8	99.4
	$ax_{3,nb}$	96.9	97.1	93.9	94.4	98.8	99.4
4	ax	96.8	97.2	93.8	94.5	98.7	99.2
	ax_{small}	88.1	90.1	78.8	81.9	85.8	90.7
	ax_4	96.6	97.0	93.5	94.1	98.4	99.2
	$ax_{4,nb}$	96.9	97.2	94.0	94.6	98.7	99.4
5	ax	96.0	96.5	92.3	93.2	98.6	98.9
	ax_{small}	86.7	88.6	76.5	79.6	85.4	89.9
	ax_5	94.1	94.7	88.9	90.0	88.6	92.6
	$ax_{5,nb}$	94.6	95.1	89.7	90.7	90.2	94.5
all	ax	96.2	96.6	92.6	93.4	98.2	99.0
	ax_{small}	86.8	86.9	76.6	76.8	85.2	87.6
	ax_{1-5}	95.9	96.4	92.1	93.0	96.7	98.7
	ax_{nb}	96.1	96.6	92.5	93.4	97.1	99.0

5.6 Slice to Slice Result Propagation

Results on the 3-slice U-Net implementing predictions of the previous and the next slice are found in Table 3.

Table 3: Test runs on 3-slice model expecting prediction for *(n-1),* original axial slice and prediction for *(n+1)*.

model	DSC	DSC_{med}	JI	JI_{med}	NSD	NSD_{med}
ax	96.2	96.6	92.6	93.4	98.2	99.0
ax_{ppp}	95.2	95.6	90.8	91.5	95.1	98.6
ax_{pop}	97.0	97.3	94.1	94.7	98.7	99.4
ax_{top}	98.6	98.5	97.2	97.0	99.9	99.9
ax_s	96.8	96.9	93.8	93.9	96.2	99.3
ax_{spop}	97.2	97.3	94.5	94.7	98.0	99.2
sag_{pop}	97.1	97.1	94.4	94.4	97.2	99.1
ax_c	96.5	96.5	93.2	93.3	97.9	98.6
ax_{cpop}	96.9	97.1	94.0	94.4	98.3	99.1
cor_{cpop}	96.9	97.0	93.9	94.1	98.2	99.0

The model is thereby trained to get the intensity profile for slice *n* and a first rough prediction for the slices *n-1* and *n+1*. In Table 3 there are test runs for three predictions as ax_{ppp}, the expected input ax_{pop} together with neighbouring predictions and ground truth for previous (ax_{top}). Furthermore, the reconstructed sagittal and coronal slices are tested, too, utilizing the same model. For the coronal and sagittal view, the axial 3-slice model (ax_{spop}, ax_{cpop}) leads to similar improvements after reconstruction to axial view as applying specific trained 3-slice models for coronal and sagittal before the reconstruction (sag_{spop}, cor_{cpop}), cf. Fig. 7.

5.7 Hybrid Position Model of Axial, Coronal and Sagittal Segmentation

Combining the particular results from axial, coronal and sagittal the overall quality of results gets improved for the a priori position model and a U-Net trained for combination.

Table 4: Quality of results for the segmentations *ax*, ax_c and ax_s is improved by combining with average (*AVG*), position model (*PosW*) or U-net model trained for combination (*model*). As input, the pre-classified slices without (*a, s, c*) and with 3-slice improvement (*a', s', c'*) are applied.

model	DSC	DSC_{med}	JI	JI_{med}	NSD	NSD_{med}
ax	96.2	96.6	92.6	93.4	98.2	99.0
ax_s	96.8	96.9	93.8	93.9	96.2	99.3
ax_c	96.5	96.5	93.2	93.3	97.9	98.6
$AVG_{a,c,s}$	97.2	97.3	94.6	94.7	99.1	99.4
$PosW_{a,c,s}$	97.2	97.3	94.6	94.7	99.1	99.4
$model_{a,c,s}$	97.5	97.6	95.2	95.2	99.3	99.5
$AVG_{a',c',s'}$	97.4	97.5	94.9	95.1	99.2	99.5
$PosW_{a',c',s'}$	97.4	97.5	94.9	95.1	99.2	99.5
$model_{a',c',s'}$	97.6	97.7	95.3	95.5	99.4	99.6

Results on the entire liver dataset can be found in Table 4. Comparing the simple averaging (*AVG*) and the complex position-based a priori model (*PosW*), the results are almost equal.

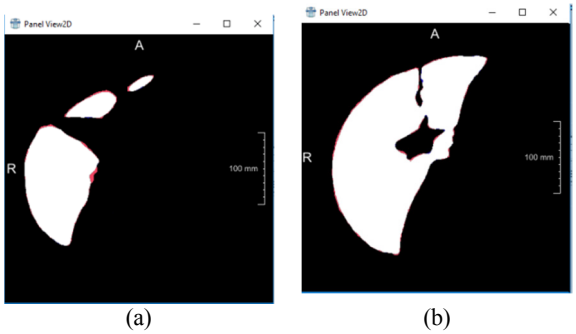

(a) (b)

Figure 14: Axial view of segmentation mismatch of slice 88 and 135 of dataset #111 for model $model_{a',c',s'}$ (a-b). The 3-slice model and combination of orthogonal views corrects the error ($model_{a',c',s'}$) of *ax* model, c.f. Fig. 12.

It is shown that U-net models are applicable for result migration too and highest accuracy is achieved for utilizing both, the 3-slice-improvement and the combination of the orthogonal views, c.f. Fig. 14 (a-b) for slices 88 and 135 of dataset #111.

5.8 Comparison to Other Approaches

The highest achieved accuracy in this paper is to be quantified with *DSC=97.59*, *JI=95.29* and *NSD=99.37* for $PosW_{a',c',s'}$.

A similar slice-based approach utilizing LevelSets for result propagation and a Statistical Shape Model for initial parametrization achieved an average *JI=93.6±3.3* and a volume match of *96.82±1.72%* (Zwettler et al. 2009). At the medical decathlon 2018, the top team achieved *DSC=0.95* and *NSD=0.98* evaluated for L1 region utilizing a nnU-Net (Isensee et al. 2019).

6 DISCUSSION

With precise pre-processing and post-processing, the domain of 3D segmentation in medicine can be addressed with 2D slice-by-slice models, too approaching similar level of quality. Classification with 2D models has some significant advantages with respect to calculation power required for model training and memory consumption. Furthermore, for user-centric approaches in the medical domain, the interaction with 2D slices is more common with a broader range of interaction paradigms.

Surprisingly the sectional models did not pay of as expected. It was shown that this fact results from the reduced amount of testing data. Thus, if a sufficient amount of slices is available, splitting into sectors is a reasonable strategy, training only on a subset of the axial shapes and positions besides the intensity profile. With the data augmentation strategy presented in this paper, the lack in training data could not be compensated. Instead, real medical image data or results of GANs should be utilized.

With the 3-slice model, the perfect basis for user-centric and interactive post-processing is provided. In this paper it was shown that the improved results can be propagated from slice to slice. Nevertheless, the $axial_{pop}$ model perfectly worked out for improving the initially segmented slices at similar accuracy compared to the particular models (sag_{spop}, cor_{cpop}). Marginal incorporation of a mini 3D-subvolume of 3 slices significantly improved results. In future incorporating 5 or 7 slices will be investigated, possibly a higher step increment will allow further improvement.

The combination of the axial and reconstructed coronal and sagittal results is a crucial point. As for all positions two of the main views lead to robust results, it is not a huge surprise that a simple averageing model can compete with the presented complex a priori position model. The concept, that axial is weak at caudal and cranial directions with sagittal and coronal weak at front/back and left/right respectively was proven by deeper analysis.

Nevertheless, these aspects were not corrrectltly adressed with the position-based model. The caudal and cranial sections are not only axial slices at the very begin or end as they might arise inside the volume too. Thus, it would be a better strategy to analyze the local gradients, e.g. utilizing eigenvalue analysis. If the x, y or z-gradients are high in local neighborhood, one can conclude the adapted weights for axial, coronal and sagittal then.

With the chosen ROI size of *288×352×256* it was shown that tensors for deep learning not necessarily need to be isotropic as stated in other papers.

7 CONCLUSIONS

Utilizing powerful Deep Learning as a small image processing module, most of its black box nature vanishes. If these modules are integrated into conventional image processing chains in an adequate way, significant improvements on the date pre- and post-processing become feasible.

Furthermore, it is shown that in spite of iteratively improving deep learning architectures and processing power it still might be a reasonable decision to decompose a 3D segmentation problem into slice-by-slice processing.

Future work will focus on user-centric interaction paradigms. Up to now powerful deep learning models are available for a broad community but rather as a black box. Thus, one has to accept the most often good results as they are provided by the model.

Nevertheless, in computer-based medical analytics the human diagnostician always should have powerful tools for overruling the machine made decisions. With slice-wise processing of the input volume, many human-computer interaction paradigms become realizable.

Another aspect to address in ongoing research is the genericity of this concept. Besides the parenchyma-optimized ROI dimensionality all other aspects of the model are very generic. With definition of a priori ROI and windowing, one axial sagittal, coronal model should be able to not only handle parenchyma data, but also datasets with kidney, lung, gall bladder and many

more in focus too if getting re-trained on a sufficient amount of reference data.

REFERENCES

Aggarwal, A., Vig, R., Bhadoria, S., and Dethe, C.G., 2011. Role of Segmentation in Medical Imaging: A Comparative Study. In: *Int. Journal of Comp. Applic. 29(1)*.

Amorim, P.H.A., Chagas, V.S., Escudero, G.G., Oliveira, D.D.C., Pereira, S.M., Santos, H.M., and Scussel, A.A., 2017. *3D U-Nets for Brain Tumour Segmentation*. In: MICCAI 2017 BraTS Challenge. In: Proc. of the MICCAI 2017.

Arik, S.O., Chrzanowski , M., Coates, A., Diamos , G., Gibiansky, A., Kang, Y., Li, X., Miller, J., Raiman, J., Sengupta, S., and Shoeybi , M., 2017. *Deep voice: Real time neural text to speech*. In: ICML 2017

BIR, 1986. *ANALYZE™ Header File Format*, available from http://www.grahamwideman.com/gw/brain/analyze/formatdoc.htm, last visted 11.9.2019.

Chen, C., Liu, X., Ding, M., Zheng, J., and Li, J., 2019. 3D Dilated Multi-Fiber Network for Real-time Brain Tumor Segmentation in MRI. In: *CoRR*, available from https://arxiv.org/pdf/1904.03355.pdf, last visited 1.10.2019.

Christensen, A., and Wake, N., 2018. *Wohler Report: Medical image processing software*, Available from http://www.wohlersassociates.com/medical2018.pdf , last visited 1.10.2019 .

Cicek, Ö., Abdulkadir, A., Lienkamp, S.S., Brox, T., and Ronneberg, O. 2016. *3D U-Net: Learning Dense Volumetric Segmentation from Sparse Annotation*. In: MICCAI 2016.

Cootes, T.F., Taylor, C.J., Cooper, D.H., and Graham, J., 1992. *Training Models of Shape from Sets of Examples*. In Proc. of the British Machine Vision Conference, 9-18., Leeds, U.K.

Cootes, T.F., Edwards, G.J., and Taylor, C.J., 1998. *Active Appearance Models*. In Proc. of the 5th Europ. Conf. on Computer Vision, 484- 498. June 2-6, Freiburg, Germany.

DFWG, 2005. *NIFTI - Neuroimaging Informatics Technology Initiative*, available from https://nifti.nimh.nih.gov/, last visited 11.9.2019

Dice, L.R., 1945. Measures of the Amount of Ecologic Association Between Species. In: *Ecology*. 26 (3).

Frid-Adar, M., Diamant, I., Klang, E., Amitai, M., Goldberger, J., and Greenspan, H., 2018. GAN-based synthetic medical image augmentation for increased CNN performance in liver lesion classification. In: *Neurocomputing*, pp. 321-331.

Goodfellow , I.J., Pouget Abadie , J., Mirza, M., Xu, B., Warde Farley, D., Ozair, S., Courville, A., and Bengio, Y., 2014. *Generative Adversarial Nets*. In Proc. of the 27th Int. Conf. on Neural Information Processing Systems, vol. 2.

Hochreiter, S., and Schmidhuber, J., 1997. Long Short-Term Memory. In: *Neural Computation 9(8)*, pp. 1735-1780.

Huang, C., Han, H., Yao, Q., Zhu, S., and Zhou, S.K., 2019. *3D U^2-Net: A 3D Universal U-Net for Multi-Domain Medical Image Segmentation*. In: Proc. of the MICCAI 2019.

Isensee, F., Petersen, J., Kohl, S.A.A., Jäger, P.F., and Maier-Hain, K.H., 2019. nnU-Net: Breaking the Spell on Successful Medical Image Segmentation. In: *CoRR*.

Jaccard, P., 1912. The Distribution of the flora in the alpine zone, In: *New Phytologist*, 11.

Kingma, D.P., and Ba, J.L., 2014. *Adam : A method for stochastic optimization*. In: Int. Conf. on Learning Representations (ICLR), available from https://arxiv.org/abs/1412.6980, last visited 1.10.2019.

Laplante, P.A. (ed.), 2019. *Encyclopedia of Image Processing*. In: CRC Press/Taylor & Francis Publishing.

McInerney, T., and Terzopoulos, D., 1996. Deformable Models in Medical Image Analysis : A Survey. In *Medical Image Analysis 1 (2)*: pp. 91-108.

MedDecathlon, 2018. *MSD-Ranking Scheme*, available from: http://medicaldecathlon.com/files/MSD-Ranking-scheme.pdf, last visited 19.9.2019.

Meine, H., Chlebus, G., Ghafoorian, M., Endo, I., and Schenk, A., 2018. *Comparison of U-net-based Convolutional Neural Networks for Liver Segmentation in CT*. In: Computer Vision and Pattern Recognition, available from https://arxiv.org/abs/1810.04017, last visited 1.10.2019.

Rajagopalan, S., Karwoski, R.A., Robb, R.A., Ellis, R.E., and Peters, T.M., 2003. *Shape-Based Interpolation of Porous and Tortuous Binary Objects*. In: MICCAI 2003, pp. 957-958.

Robb, R.A., Hanson, D.P., Karwoski, R.A., Larson, A.G., Workman, E.L. and Stacy, M.C., 1989. Analyze: a comprehensive, operator-interactive software package for multidimensional medical image display and analysis. In: *Comput Med Imaging Graph* 13(6): 433–454.

Ronneberg, O., Fischer, P., and Brox, T., 2015. *U-Net: Convolutional Networks for Biomedical Image Segmentation*. In: MICCAI 2015, Springer, LNCS, Vol.9351: 234—241.

Simpson, A., Antonelli, M., Bakas, S., Bilello, M., Farahani, K., Ginneken, B., Kopp-Schneider, A., Landman, B., Litjens, G., Menze, B., Ronneberger, O., Summers, R., Bilic, P., Christ, P., Do, R., Gollub, M., Golia-Pernicka, J., Heckers, S., Jarnagin, W. and Cardoso, M.J., 2019. *A large annotated medical image dataset for the development and evaluation of segmentation algorithms*. In CoRR.

Squelch, A., 2018. 3D printing and medical imaging. In: *Journal Med Radiat Sci. 65(3)*.

Stegmaier, J., 2017. *New Methods to Improve Large-Scale Microscopy Image Analysis with Prior Knowledge and Uncertainty*. In: KIT Scientific Publishing, Karlsruhe.

Strakos, P., Jaros, M., Karasek, T., Kozubek, T., Vavra, P., and Jonszta, T., 2015. Review of the Software Used for 3D Volumetric Reconstruction of the Liver. In: *Int. Journal of Computer and Information Engineering 9(2)*.

Van Biesen, W., Sieben, G., Lameire, N., and Vanholder, R., 1998. Application of Kohonen neural networks for the non-morphological distinction between glomerular and tubular renal disease. In: *Nephrol Dial Transplant 13(1)*, pp. 59-66

Viola, P., and Jones, M., 2001. *Rapid Object Detection using a Boosted Cascade of Simple Features*. In: Conf. on Computer Vision and Pattern Recognition 2001

Yang, D., Xu, D., Zhou, S.K., Georgescu, B., Chen, M., Grbic, S., Metaxas, D., and Comaniciu, D., 2017. *Automatic Liver Segmentation Using an Adversarial Image-to-Image Network*. In: MICCAI 2017.

Yi, X., Walia, E., and Babyn, P., 2019. Generative Adversarial Network in Medical Imaging: A Review. In: *Medical Image Analysis vol. 58*.

Zhang, J., and Wang, X.W. 2011. The application of feed forward neural network for the X ray image fusion. In: *J. Phys*.

Zwettler, G., and Backfrieder, W., 2013. *Generic Model-Based Application of Modular Image Processing Chains for Medical 3D Data Analysis in Clinical Research and Radiographer Training*. In: Proc. of IWISH 2013, pp. 58-64

Zwettler, G., Backfrieder, W., Swoboda, R., and Pfeifer, F., 2009. *Fast Fully-automated Model-driven Liver Segmentation Utilizing Slicewise Applied Levelsets on Large CT Data*. In: Proc. of the 21st EMSS 2009, pp. 161-166.